Journal of
Materials Chemistry C

PAPER

View Article Online
View Journal

Check for updates

Cite this: DOI: 10.1039/d5tc03820k

Pure and mixed {Nd/Yb} carborane-based metal–organic frameworks integrating slow magnetic relaxation, magnetocaloric effect and NIR emission

Xiaoming Liu,[a] Ana Arauzo,[b] Sara Fuertes,[c] José Giner Planas*[a] and Elena Bartolomé*[a]

Received 24th October 2025,
Accepted 15th March 2026

DOI: 10.1039/d5tc03820k

rsc.li/materials-c

Multi-lanthanide metal–organic frameworks (MOFs) offer a flexible route for designing multifunctional materials. Here we report a carborane-based isostructural series of MOFs of formula $\{[(\mathrm{Nd}_y\mathrm{Yb}_{1-y})_3(m\mathrm{CB}\text{-}\mathrm{L})_4(\mathrm{NO}_3)(\mathrm{DMF})_x]_n\cdot\mathrm{Solv}\}$, including the homometallic Nd (y = 1) and Yb (y = 0) compounds and a mixed Nd/Yb analogue (y = 0.44). Magnetic, magnetocaloric and near-infrared (NIR) optical properties were investigated by dc/ac magnetometry, X-ray absorption spectroscopy (XAS), X-ray magnetic circular dichroism (XMCD), and photoluminescence. Nd^{3+} and Yb^{3+} yield MOFs combining slow relaxation of the magnetization ($U/k_B \sim 19$ K), cryogenic magnetocaloric response ($-\Delta S_m \sim 1.6$ R at 5 T, 1.8 K) and ion-centered NIR luminescence. Notably, the mixed Nd/Yb MOF further extends this multifunctionality by exhibiting dual NIR emission at 998 nm and 1060 nm arising from partial Nd → Yb energy transfer. These results underscore carborane ligands as effective blocks for engineering multi-lanthanide frameworks, and highlight {Nd/Yb} MOFs as multifunctional materials for quantum technologies, optical communication, and cryogenic cooling.

Introduction

Metal–organic frameworks (MOFs), composed of metal ions and organic linkers arranged in crystalline, porous structures, have gained widespread attention due to their applicability in catalysis,[1,2] gas storage[3] and separation,[4,5] biomedical applications,[6] magnetism,[7–9] *etc.* In particular, lanthanide-based MOFs (Ln-MOFs) exhibit unique magnetic, electronic, and optical properties, making them highly attractive for advanced technologies, including luminescence,[10–12] anticounterfeiting,[13] sensors,[14–16] switching,[17] thermometry,[18] magnetic refrigeration,[19–22] information storage and processing.[23–34] These properties arise from the intrinsic electronic characteristics of 4f ions, which endow them with significant anisotropy, strong spin–orbit coupling, and well-defined optical transitions. Hence, Ln(III) ions are ideal candidates for single-molecule magnets (SMMs), exhibiting magnetic stability and quantum-tunneling effects,[35–37] while some also demonstrate excellent visible (VIS) and near-infrared (NIR) emission properties.[13,38–40] Furthermore, the magnetocaloric effect (MCE) observed in Ln(III) materials makes them promising for sustainable, low temperature cooling.[19–22] While Gd(III), with its high spin (S = 7/2) and negligible orbital contribution (L = 0), is the preferred ion to maximize entropy change, recent studies suggest that alternative anisotropic lanthanides can serve to optimize MCE performance under lower magnetic field variations[38] and extend the operational temperature range.[39–41] Interestingly, certain Ln-MOFs integrate multiple functionalities, such as magnetism coupled with luminescence,[42,43] or proton conductivity.[44,45]

In addition, the incorporation of multiple metals in multivariate (MTV) MOFs is emerging as an interesting approach to create a range of multifunctional materials, with novel, additive or synergistic properties.[46–48] While multi-metallic MTV MOFs containing up to ten different transition metals have been studied in depth,[48–53] multi-lanthanide MOFs remain relatively unexplored,[54] as the synthesis of these materials without the problem of segregation is not easy. Most reports on mixed Ln-MOFs (commonly incorporating Eu/Tb,[20,55,56] but also La/Eu,[57] Gd/Eu,[55,57–59] Gd/Tb,[55,58,59] Gd/Sm,[59] Eu/Gd/Tb[60–62] or Ce/Eu/Tb[58]), have targeted colour tuning, white-light emission, or ratiometric luminescent temperature sensing,[63–66] while

---

[a] *Institut de Ciència de Materials de Barcelona (ICMAB)-CSIC, Campus UAB, 08193-Bellaterra, Spain. E-mail: jginerplanas@icmab.es, ebartolome@icmab.es*

[b] *Departamento de Física de la Materia Condensada, Instituto de Nanociencia y Materiales de Aragón (INMA), CSIC-Universidad de Zaragoza, 50009 Zaragoza, Spain*

[c] *Departamento de Química Inorgánica, Facultad de Ciencias, Instituto de Síntesis Química y Catálisis Homogénea (ISQCH), CSIC-Universidad de Zaragoza, Pedro Cerbuna 12, Zaragoza, 50009, Spain*

only a handful of Gd/Ln-based MOFs (Ln = Tb, Dy or Eu, Tb/Eu) have been investigated for MCE enhancement under low fields (< 2 T),[39] expanded operational temperature ranges,[41] or multifunctional MCE, SMM, and VIS-emission properties.[67] Recently, polynuclear Gd/Tb/Eu MOFs have emerged as promising candidates for optical tagging, enabling orthogonal encoding through independently tunable luminescence lifetimes and compositions.[68]

Remarkably, in our recent work we have demonstrated that the bulky and acidic character of the carborane linker *m*CB-L = 1,7-di(4-carboxyphenyl)-1,7-dicarba-*closo*-dodecaborane, facilitates the synthesis of multivariate MOFs incorporating diverse lanthanide combinations. Icosahedral carboranes, a commercially accessible class of boron-rich clusters, are renowned for their exceptional stability,[69–71] high hydrophobicity,[70–76] and unique electronic structure, making them intriguing inorganic 3D "aromatic" moieties.[77–79] This strategy has successfully produced Tb/Eu MOFs for anticounterfeiting,[13] GdLn MOFs with combined magnetocaloric and luminescent properties,[67] and the first-ever MOF incorporating eight different lanthanides.[80] Leveraging this multivariate approach, we can now engineer carborane-based MOFs with precisely tailored lanthanide combinations to explore complex magnetic phenomena and multifunctional behavior. We anticipate that application of artificial intelligence (AI) may further accelerate the discovery of novel multi-lanthanide MOFs with compelling characteristics. However, AI-driven insights rely on the prior synthesis and thorough characterization of an extensive library of multi-lanthanide MOFs to establish meaningful correlations between structure and function.

Motivated by these considerations, we focus here on the relatively underexplored Nd, Yb, and mixed Nd/Yb MOFs. Research on Ln-SMMs has primarily centered on heavy lanthanide ions, particularly Dy(III), Tb(III), and Er(III), while molecular materials based on light Nd(III) and heavy Yb(III) remain relatively scarce. A literature review of previously reported Nd(III), Yb(III), and mixed Nd/Yb metal–organic across dimensions showing SMM and/or NIR emission is provided in SI S1–S3 (Tables S1–S6).

The Nd(III) Kramers ion, characterized by its oblate electron density and $^4I_{9/2}$ ($L = 6$, $S = 3/2$, $J = 9/2$) ground state, can exhibit substantial anisotropy when an appropriate crystal field stabilizes the ground $\pm M_J$ doublet well below the first-excited level. Despite this potential, Nd-based nanomagnets are relatively rare (Table S1). Since the first reported 0D single-ion magnet (SIM), [NdTp$_3$], in 2012,[81] only a handful of field-induced Nd-SIMs[81–86] and dimeric {Nd$_2$} complexes[87–89] have been documented, with [NaNd(W$_5$O$_{18}$)$_2$]$_9$ exhibiting the highest thermal barrier energy ($U/k_B = 73.9$ K at 0.1 T).[82] Additionally, some 1D polymers[90,91] displaying magnetic relaxation have been identified, with {Nd(α-fur)$_3$(H$_2$O)$_2$}$_n$ currently holding the activation energy record ($U/k_B = 121$ K at 0.12 T).[90] Beyond low-dimensional nanomagnets, Nd(III) has also been incorporated into MOFs, offering potential for multifunctional materials. Several Nd-based MOFs have been synthesized,[92] mostly targeting catalysis,[93] while magnetically diluted [N(C$_2$H$_5$)$_4$][Nd$_x$La$_{100-x}$(CAN)$_2$(H$_2$O)] MOFs have recently emerged as promising platforms for organizing qubits.[94] In addition to its magnetic properties, Nd(III) is also valued for its near-infrared (NIR) luminescence (Table S2), which makes it suitable for optical communication, bioimaging, and sensing applications.[95] However, studies on the dual magneto-optical properties of Nd-MOFs are limited, with most reports focusing either on basic dc magnetometry or NIR characterization.[96–98] Only a few multifunctional Nd-MOFs have been described, including the chiral luminescent 2D nanomagnet {Nd$^{III}_4$(H$_2$O)$_{17}$(pzdo)$_5$[M^{IV}(CN)$_8$]$_3$}·9H$_2$O,[99] and the 3D MOF [Nd^{III}(H$_2$O)$_3$][M^I(CN)$_2$]$_3$ (M^I = Ag, Au), which exhibits slow magnetic relaxation (energy barriers of 18.8 and 25.6 K at 0.2 T) alongside bluish emission.[100] Even fewer MOFs display both slow relaxation and NIR emission; notable examples include {[Nd$_2$(2,5-pzdc)$_3$(H$_2$O)$_4$]·6H$_2$O,[101] and [Nd$_2$(ant)2((NH$_2$)$_2$-bdc)-(DMF)$_4$]·2DMF}$_n$.[102]

On the other hand, Yb(III) features a prolate f-electron density and a Kramers $^2F_{7/2}$ ($L = 3$, $S = 1/2$, $J = 7/2$) ground state. Following early theoretical prediction[103] and experimental confirmation of SMM behavior in mononuclear Yb complexes,[104] studies expanded to dinuclear SMMs[105,106] and 1D polymeric compounds (Table S3). Despite the relatively weak magnetic moment of Yb^{3+}, Yb-based SIMs have been key to probing how equatorial coordination enhances anisotropy in prolate lanthanides,[107] contrasting with oblate ions such as Dy^{3+}, Tb^{3+}, and Er^{3+}. A notable example is Yb[trensal], where the coordination environment features a pronounced equatorial plane formed by four donor atoms. For similar reasons, octahedral Yb^{3+} complexes have also shown significant SMM behavior.[108,109] Beyond magnetism, Yb^{3+} compounds show pronounced NIR luminescence,[110] which is relevant both for applications (*e.g.*, medicine, telecommunications) and fundamental studies (Table S4). Emission spectroscopy provides insight into ground-state multiplet splitting, allowing correlation with magnetic data. This has been applied to mono- and dinuclear SMMs to assess whether relaxation follows an Orbach mechanism,[111] or alternative pathways like Raman or direct processes prevail.[108,112,113] Furthermore, Gavrikov *et al.*[114] recently reviewed 1D polymeric Yb-based SMMs, highlighting how magnetic interactions can negatively affect SMM performance.

Mixed Nd/Yb compounds are attracting increasing interest in the search for novel photophysical phenomena and applications based on Ln-to-Ln' energy transfer (ET). Site-resolved di[115] and trinuclear[116,117] heterometallic molecules have provided insights into this ET mechanism. Nd/Yb-containing materials are being explored as ratiometric luminescent thermometers, particularly for biomedical applications (Table S5). This is driven by the fact that both Nd^{3+} and Yb^{3+} ions exhibit excitation and emission bands within the biological optical transparency windows, enabling minimized tissue absorption, scattering, and autofluorescence—key factors for effective deep-tissue imaging and thermal sensing.[118] In particular, Nd/Yb-MOFs have emerged as promising NIR-emissive platforms, offering modular design, tunable emission, permanent porosity, and multifunctionality. Recent efforts have focused on understanding[119] and enhancing $Nd^{3+} \rightarrow Yb^{3+}$ ET efficiency towards optimizing sensing performance.[120–122] Furthermore, the combination of Nd and Yb MOFs[117] has enabled the fabrication of multi-emissive NIR core–shell architectures, such as Nd-MOF@Yb-MOF@SiO_2@Fe_3O_4 nanoparticles, serving as luminescent thermometers and sensing of felodipine.[110] On the other hand, the magnetic properties of mixed Nd/Yb MOFs remain largely unexplored. Only recent studies have begun exploring Nd/Yb-based MOFs as bifunctional materials that combine NIR luminescence with field-induced single-molecule magnet (SMM) behavior. Such dual-response systems represent a promising frontier for developing magneto-optical materials with advanced sensing and data storage capabilities. Notably, the 3D MOF $[Nd_{1-x}Yb_x(2,2'\text{-bpdo})_2(H_2O)][Cu_2I(CN)_5]\cdot 5H_2O$ demonstrated the coexistence of NIR-based thermometric behavior, with tunable operational temperature ranges enabled by Yb^{3+} content variation, second-harmonic generation (SHG), and field-induced SMM behavior occurring *via* Raman and direct relaxation processes.[123] (Table S6). These findings highlight the untapped potential of Nd/Yb-based MOFs for combined sensing, photonic, and magnetic applications.

Overall, the above overview highlights that despite growing interest in multifunctional, multimetallic MOFs, Nd/Yb MOFs remain largely unexplored. In this work, we address this gap by extending our carborane-based multivariate MOF platform to the Nd/Yb pair. We report the synthesis and comprehensive magneto-thermal and optical characterization of carborane-based MOFs with general formula $\{[(Nd_yYb_{1-y})_3(m\text{CB-L})_4(NO_3)(DMF)_x]_n\cdot\text{Solv}\}$, including homometallic (Nd, Yb) and mixed Nd/Yb analogues. Their properties are investigated using a combination of dc and ac magnetometry, X-ray absorption spectroscopy (XAS), and X-ray magnetic circular dichroism (XMCD), and NIR luminescence spectroscopy. We discuss the emergence of multifunctional behavior in these materials. By elucidating the interplay between magnetism, optical properties, and thermal effects, this work contributes to advancing the understanding of multifunctional Nd/Yb MOFs and the broader field of magnetic multi-lanthanide MOFs.

Experimental section

Synthesis

All chemicals were of reagent-grade quality. They were purchased from commercial sources and used as received. 1,7-Di(4-carboxyphenyl)-1,7-dicarba-*closo*-dodecaborane ligand ($m\text{CBH}_2\text{L}$) was synthesized by a slight modification of a literature procedure.[124]

$\{[(Nd_yYb_{1-y})_3(m\text{CB-L})_4(NO_3)(DMF)_x]_n\cdot\text{Solv}\}$ (y = 1, ***m*CB-Nd**; y = 0, ***m*CB-Yb**; y = 0.44, ***m*CB-NdYb**) compounds were synthesized following a previously described procedure.[80] In a typical preparation, $m\text{CB-H}_2\text{L}$ (0.03 mmol) and $Ln(NO_3)_3$ (0.02 mmol; Ln = Nd, Yb, or Nd and Yb) were added to a mixture of DMF (0.5 mL)/methanol (1.5 mL)/H_2O (0.3 mL) and sonicated until complete dissolution of all reagents. The above mixture was transferred to an 8-dram vial and heated at 95 °C in an oven for 48 h. Needle like white crystals were collected and washed with DMF. Yield based on the Ln ions: 57.4% for ***m*CB-Nd**, 60.1% for ***m*CB-Yb**, 38% for ***m*CB-NdYb**. IR (ATR; selected bands; cm^{-1}): ***m*CB-Nd**, 2596 (BH), 1655 (C═O from DMF); 1589, 1537, 1398 ($\mu(COO^-)$); ***m*CB-Yb**, 2600 (BH), 1658 (C═O from DMF); 1590, 1535, 1416 ($\mu(COO^-)$); ***m*CB-NdYb**, 2597 (BH), 1657 (C═O from DMF); 1590, 1542, 1407 ($\mu(COO^-)$); ICP (wt%): ***m*CB-NdYb**, Nd (8.1 ± 0.1), Yb (12.3 ± 0.1): $\{[Nd_{1.32}Yb_{1.68}(m\text{CB-L})_4(NO_3)(DMF)_x]_n\cdot\text{Solv}\}$.

Instruments and characterization

Attenuated total reflection Fourier transform infrared (ATR-FTIR) spectra were acquired using a PerkinElmer Spectrum One spectrometer equipped with a Universal ATR accessory. The spectral range spanned 4000–650 cm^{-1} with a resolution of 2 cm^{-1}. Elemental composition (wt% CHN) was determined using a Thermo (Carlo Erba) Flash 2000 Elemental Analyzer. Powder X-ray diffraction (PXRD) patterns were collected at ambient temperature using a Siemens D-5000 diffractometer, operating with Cu Kα radiation (λ = 1.5418 Å, 35 kV, 35 mA) and a step size of 0.02°. Inductively Coupled Plasma–Mass Spectrometry (ICP–MS) was performed on an Agilent 7700x instrument.

Morphological and optical characterization was conducted *via* scanning electron microscopy (SEM) on a QUANTA FEI 200 FEGESEM and optical microscopy using an Olympus BX52. Solid-state UV-Vis-NIR spectra were recorded on a JASCO V-780 spectrophotometer, covering the spectral range of 200–1600 nm.

Magnetic measurements were performed using a quantum design MPMS3 SQUID magnetometer equipped with a 7 T superconducting magnet. Direct current (dc) magnetization was measured from 1.8 to 300 K on powder samples dispersed in Daphne oil to mitigate grain alignment effects. The $M(H)$ isotherms used for MCE analysis were recorded under quasi-static conditions (no detectable hysteresis was observed at 1.8 K), supporting the validity of the Maxwell procedure. Ac susceptibility was assessed between 1.8 and 9.0 K under an oscillating field of $\mu_0H_{ac} = 4.1 \times 10^{-4}$ T and static fields up to μ_0H_{dc} = 2.5 T, with the frequency ranging from f = 0.1–1000 Hz. Complementary ac susceptibility data in the 10–10 000 Hz range were obtained using a quantum design PPMS.

X-ray absorption spectroscopy (XAS) and X-ray magnetic circular dichroism (XMCD) studies at the $M_{4,5}$ edges of Nd and Yb were conducted at the BOREAS beamline at the ALBA synchrotron. Powdered samples were finely ground, pressed onto indium foil, and mounted on the cold finger for low-temperature measurements (5.0 ± 0.5 K). Spectra were recorded in total electron yield (TEY) detection mode using 90% circularly polarized light. The XMCD ($\mu^- - \mu^+$) and XAS ($\mu^+ + \mu^-$)/2 spectra at 6 T were averaged from eight scans acquired under right- (μ^+) and left-handed (μ^-) circular polarization. Field-dependent XMCD(H) cycles were recorded by tracking the resonant M_5 peak while sweeping the magnetic field from 6 T to −6 T at a rate of 2 T min^{-1}.

The photoluminescence experiments were carried out on neat solid samples placed in quartz tubes with an internal diameter of 4 mm at room temperature. Steady-state photoluminescence measurements were recorded in a FluoTime 300 spectrofluorometer (PicoQuant GmbH) equipped with a NIR-PMT detector (Hamamatsu H10330C-75) using a 300 W Xenon lamp. Excitation spectra were recorded at the energy (λ_{em}) at which the emission spectra presented the most intense peak for each lanthanide. Time-resolved measurements were recorded with a 375 nm Picosecond Laser Diode as excitation source and using the EasyTau II software package (PicoQuant GmbH). Data analysis was performed using the built-in software FluoFit (PicoQuant GmbH).

Results and discussion

Syntheses and structure

Homo-metallic $\{[(\mathrm{Ln})_3(m\mathrm{CB\text{-}L})_4(\mathrm{NO}_3)(\mathrm{DMF})_y]_n\cdot\mathrm{Solv}\}$, with Ln = Nd (***m*CB-Nd**), Ln = Yb (***m*CB-Yb**), and hetero-metallic $\{[(\mathrm{Nd}_{1.32}\mathrm{Yb}_{1.68})_3(m\mathrm{CB\text{-}L})_4(\mathrm{NO}_3)(\mathrm{DMF})_y]_n\cdot\mathrm{Solv}\}$, (***m*CB-NdYb**) were synthesized as white crystals *via* solvothermal reactions in a DMF/methanol/H_2O mixture at 95 °C for 48 h (see Experimental Section for details). The materials were comprehensively characterized using several techniques, including powder X-ray diffraction (PXRD), Fourier transform infrared spectroscopy (FT-IR, Fig. S1), inductively coupled plasma mass spectrometry (ICP–MS, see Experimental Section), scanning electron microscopy combined with energy-dispersive X-ray spectroscopy (SEM-EDX, Fig. 1), and thermogravimetric analysis (TGA, Fig. S2), all of which yielded results consistent with the previously reported family of isostructural materials.[13,80] PXRD data, Fig. 1c, confirm that all {Nd/Yb} MOFs are isostructural with previously mono- and multi-metal MOFs of the same family (Fig. S3).[13,80] Given the structural similarity, we provide only a brief overview relevant to understanding the magnetothermal and optical properties of the novel mixed MOFs. The 3D structure (Fig. 1a and b) consists of 1D chains of Ln(III) cations aligned along the *b* axis, that are interconnected by carborane dicarboxylic linkers to form the extended structure. Each chain comprises three crystallographically distinct Ln(III) sites (Ln1, Ln2, Ln3; Fig. 1b), which are repeated along the chain, with an intra-chain metal distance of *ca.* 4.6–5.3 Å.[13,80] The arrangement of the carborane linkers results in two characteristic inter-chain separations of approximately 11 Å and 17 Å.

Scanning electron microscopy (SEM) reveals that the {Nd/Yb} MOF crystals exhibit a morphology consistent with

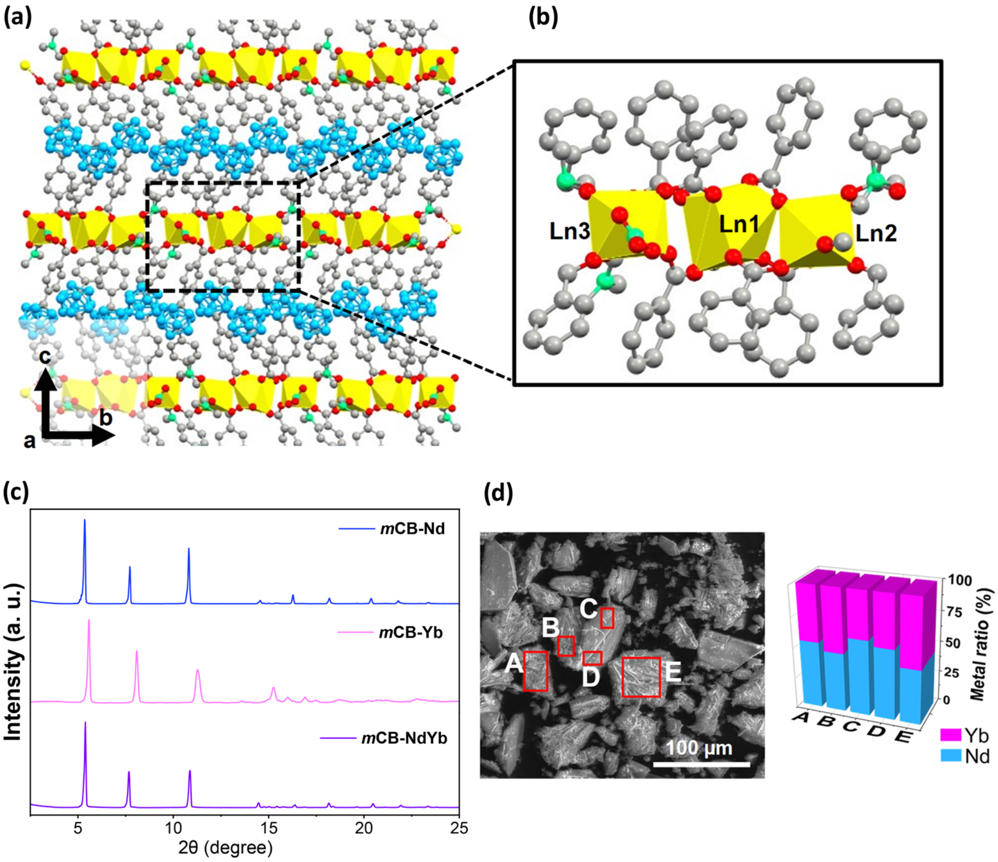

Fig. 1 Structural characterization of carborane-based {Nd/Yb} MOFs. (a) A view of the extended 3D framework for this MOF family along the *a*-axis, showing the Ln 1D-chains running along the *b*-axis, formed by three sites (Ln1, Ln2, Ln3) with non-equivalent coordination environments and the carborane linker *m*CB-L (b); colour code: Ln (yellow), O (red), B (blue), C (grey); N (green); H atoms and DMF molecules are omitted for clarity. (c) Experimental powder X-ray diffraction patterns for ***m*CB-Nd**, ***m*CB-Yb** and ***m*CB-NdYb**. (d) SEM images of mixed ***m*CB-NdYb** MOF and EDX analysis of point scans of the Ln metals on the indicated positions in the crystals.

previously reported structures (Fig. 1d).[13,80] Furthermore, EDX measurements at multiple points across the crystals confirm a uniform distribution of Ln ions, indicating the absence of phase segregation and supporting the homogeneous multi-metallic MTV MOF composition.[54]

Magnetic and magnetocaloric properties

The static magnetic behavior and magnetocaloric properties of all {Nd/Yb} MOFs were examined through SQUID magnetometry. Measurements included the temperature-dependent susceptibility product, $\chi T(T)$, under 0.1 T, and field-dependent magnetization, $M(H)$, between 1.8 K and 21 K. The magnetic entropy change, $-\Delta S_\mathrm{m}(T)$, was derived from these data using the Maxwell relation,[125] considering different field variations $\Delta B = (B_\mathrm{f} - 0)$ with $B_\mathrm{f} = 0.5$–5 T. A summary of the results is presented in Fig. 2.

For ***m*CB-Nd** MOF, the room-temperature χT product is 1.53 emu K $\mathrm{mol_{Nd}}^{-1}$, slightly lower than the free-ion limit ($\chi T_\text{free ion} = g_J^2 J(J+1)/8 = 1.64$ emu K mol^{-1} for Nd^{3+}, $g_J = 0.727$, $J = 9/2$), giving an experimental gyromagnetic factor of $g_J = 0.70$. Upon cooling, χT decreases gradually, as a result of the thermal depopulation of the excited M_J levels within the Nd(III) ground multiplet and AF interactions, reaching 0.59 emu K mol^{-1} at 1.8 K. A Curie–Weiss fit of the $1/\chi$ data above 150 K gives a rather large Curie–Weiss temperature ($\theta = -40.9$ K), likely reflecting the effect of single-ion crystal-field depopulation and/or possible overall AF coupling. Magnetization isotherms (Fig. 2b) show $M = 1.28\mu_\mathrm{B}$ per ion at 1.8 K and 5 T.

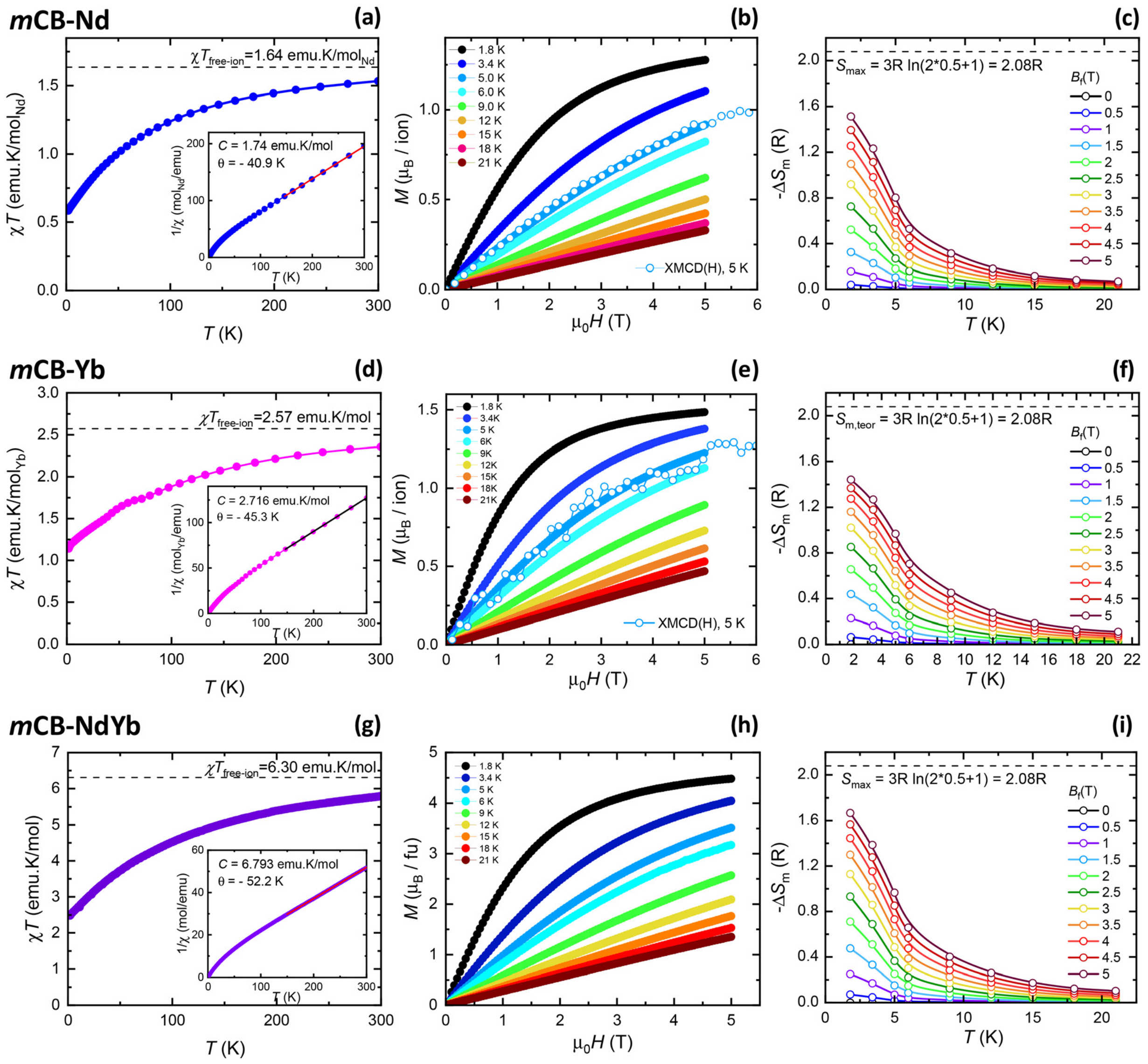

Fig. 2 Dc magnetometry and MCE properties for {Nd/Yb} MOFs (***m*CB-Nd**, ***m*CB-Yb**, ***m*CB-NdYb**). Left column (a, d, g): Temperature dependence of the susceptibility product (χT) at 0.1 T. Inset: $1/\chi$ *vs.* T data and fit to a Curie–Weiss law in the 150–300 K range; central column (b, e, h): field-dependent magnetization curves, $M(H)$, acquired between 1.8 and 21 K; right column (c, f, i): magnetic entropy change as a function of the temperature for selected magnetic field variations, $\Delta B = B_\mathrm{f} - 0$, with B_f up to 5 T.

For ***m*CB-Yb** MOF, χT at 300 K is 2.36 emu K $\text{mol}_{\text{Yb}}^{-1}$, slightly below the free-ion limit (2.57 emu K mol^{-1} for Yb^{3+}, with g_J = 1.143, J = 7/2), corresponding to g_J = 1.09. With decreasing temperature, χT decreases down to 1.14 emu K mol^{-1} at 1.8 K. The Curie–Weiss fit of the 1/χ plot at high temperatures yields θ = −45.3 K, again suggesting contributions from thermal depopulation of M_J levels and/or weak overall AF interactions. Field-dependent magnetization isotherms are displayed in Fig. 2e; the magnetization reaches 1.48μ_B per ion at 1.8 K and 5 T. It is noted that, in both ***m*CB-Nd** and ***m*CB-Yb**, the $M(H, 5\text{ K})$ curves overlap with the total per-ion magnetic moments, $m_{\text{TOT}}(H)$, extracted from XMCD(H) measurements at the Nd and Yb edges in the mixed ***m*CB-NdYb** MOF (*vide infra*).

For the mixed ***m*CB-NdYb** MOF, the χT product at room temperature (5.79 emu K mol^{-1}) matches well with the expected value based on the Nd : Yb = 1.32 : 1.68 ratio (Fig. 2g). On cooling, χT decreases to 2.48 emu K mol^{-1} at 1.8 K. A high-temperature Curie–Weiss fit gives θ = −52.3 K, which may be assigned to single-ion crystal-field depopulation and/or weak AF interactions. However, the identical sign of the Nd and Yb XMCD M$_5$ intensities measured for the mixed framework (*vide infra*) indicate any Nd–Yb AF coupling must be negligible, thus supporting the predominance of single-ion effects. The magnetization isotherms are shown in (Fig. 2h), and evidence a value of M = 4.48μ_B per fu at 1.8 K and 5 T.

The magnetocaloric properties of the three compounds are analyzed using Fig. 2 (right panel), which presents the magnetic entropy change $-\Delta S_m(T, \Delta B)$ for different field variations ΔB = (B_f − 0). In particular, we focus on results obtained for B_f = 2 T, a field strength readily achievable with permanent magnets in magnetic refrigerator applications. For ΔB = 2 T, the maximum magnetic entropy change $-\Delta S_m^{\max}$ is 0.52R (1.87 J kg^{-1} K^{-1}), 0.66R (2.26 J kg^{-1} K^{-1}), 0.71R (2.50 J kg^{-1} K^{-1}) for ***m*CB-Nd**, ***m*CB-Yb**, and ***m*CB-NdYb**, respectively. These values correspond to 25.1%, 31.7%, 34.1% of the theoretical maximum magnetic entropy available for each of the compounds, given by $S_{\max}$ = $3R\log(2 \times 0.5 + 1)$ = 2.08R. A comparison between the MCE of the homonuclear and mixed MOFs shows that the magnetic entropy change, calculated as the weighted sum of $-\Delta S_m^{\max}(H, T)$ for ***m*CB-Nd** and ***m*CB-Yb**, is slightly lower than the $-\Delta S_m^{\max}(H, T)$ curves obtained directly for ***m*CB-NdYb** (see Fig. S4), although the discrepancy ($\approx$8%) lies within the experimental uncertainty associated with the Maxwell procedure and elemental composition determination.

Reports on the magnetocaloric properties of Nd- and Yb-based MOFs remain scarce. To our knowledge, only one previous study by F. Gándara *et al.*[126] has reported the $-\Delta S_m(T)$ curves for a family of α-RPF-4 MOFs with various lanthanides, including Nd and Yb, although those data were obtained under much larger field change (ΔB = 0–7 T), precluding direct comparison with our results. As expected, the MCE performance of the ***m*CB-Nd/Yb** compounds is lower than that of their Gd-based analogue, which has a larger isotropic spin (S = 7/2) and reaches $-\Delta S_m^{\max}$ = 4.67R for ΔB = 2 T.[34] Nonetheless, the combination of magnetocaloric response, magnetic relaxation dynamics, and near-infrared (NIR) emission make them appealing as multifunctional materials. More broadly, there is increasing interest in exploring MCE in compositionally complex and multimetallic materials, motivated by the emergence of high-entropy and hybrid functional materials. Our results contribute to this effort by providing the first magnetocaloric characterization of a Nd/Yb MOF and one of the few studies on Nd- and Yb-based frameworks that also integrate SMM and optical functionalities (*vide infra*).

XAS and XMCD characterization

While SQUID magnetometry, as shown in the previous section, enables characterization of the bulk magnetic response of the mixed MOF, it cannot disentangle the separate contributions from each lanthanide. Interestingly, element-selective X-ray absorption spectroscopy (XAS) and X-ray magnetic circular dichroism (XMCD) provide direct access to the spectroscopic fingerprints and magnetic moments of individual ions within compositionally-complex materials, and is increasingly recognized as a powerful technique for the investigation of multimetallic MOFs,[67,80] In this work, XAS and XMCD were employed to assess the spectroscopic and magnetic properties of the individual lanthanide ions in the mixed ***m*CB-NdYb**. The XAS and XMCD spectra measured across the M$_{4,5}$ edges of Nd and Yb ions at 5.0 K and 6 T are shown in Fig. 3. The orbital (m_L), spin (m_s) and total magnetic moment ($m_{\text{TOT}} = m_L + m_s$) of each ion were determined from the XAS-XMCD data using the corrected sum rules for lanthanides[127,128] (Fig. 3, inset Table). The field-dependence of the total magnetic moment, $m_{\text{TOT}}(H)$, for each Ln ion was determined by following the intensity of the XMCD(H) peak at the M$_5$ edge between −6 T and 6 T, and scaling the curve with the value of m_{TOT} obtained at 6 T.

The XAS and XMCD spectra at the Neodymium M$_{4,5}$ edges exhibit the characteristic features of trivalent Nd^{3+} ion (Fig. 3a). The XAS spectrum shows a pre-peak at 972.8 eV and a main peak at 977.7 eV in the M$_5$ region, along with three distinct features (995.2, 997.3, and 999.2 eV) in the M$_4$ region. The XMCD spectrum presents a positive peak at 976.9 eV in the M$_5$ region and two negative peaks in the M$_4$ region: a minor one at 995.5 eV and a major one at 999.4 eV. For Ytterbium, the XAS spectrum displays a sharp, structureless peak at the M$_5$ edge (1519.6 eV), while the corresponding XMCD spectrum exhibits a symmetric single peak, consistent with the expected behavior of Yb^{3+} (Fig. 3b).

Fig. 3c shows the magnetic field dependence of the total magnetic moment per ion, $m_{\text{TOT}}(H)$, obtained at 3.4 K for Nd^{3+} and Yb^{3+} in ***m*CB-NdYb**. They coincide with the $M(H)$ curves measured separately in the homonuclear Nd and Yb-MOFs at the same temperature (see Fig. 2b and e). Moreover, the magnetic moment per formula unit calculated by taking a weighted linear combination (LC) of the $m_{\text{TOT}}(H)$ for each ion: $m_{(m\text{CB-NdYb})}$ = (Nd/fu) × $m_{\text{TOT}}(H)$/ion(Nd^{3+}) + (Yb/fu) × $m_{\text{TOT}}(H)$/ion(Yb^{3+}) is in excellent agreement with the magnetization curve, $M(H)$, measured by SQUID magnetometry at the same temperature.

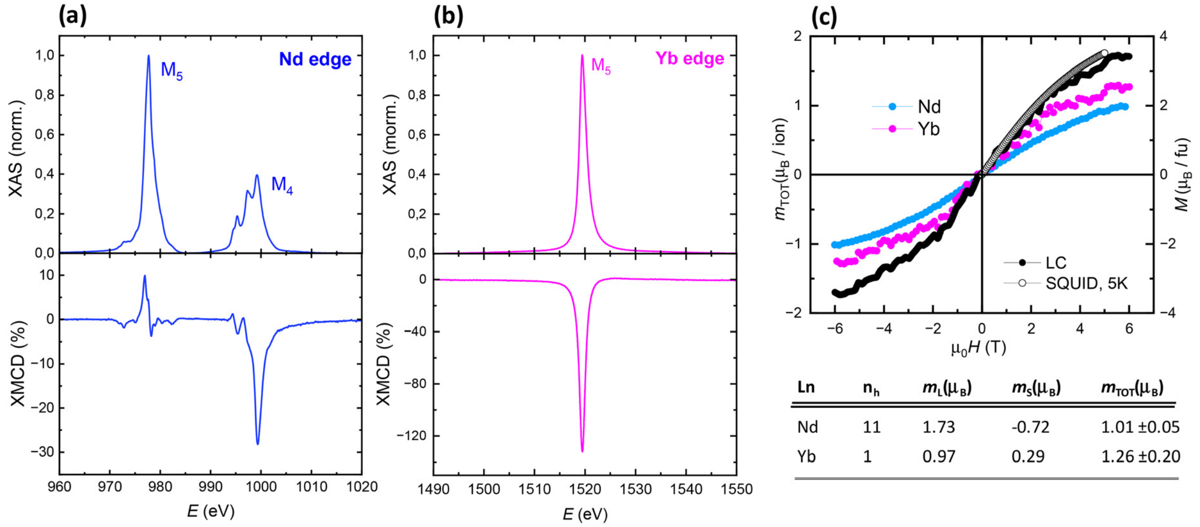

Ln	n_h	$m_L(\mu_B)$	$m_S(\mu_B)$	$m_{TOT}(\mu_B)$
Nd	11	1.73	-0.72	1.01 ±0.05
Yb	1	0.97	0.29	1.26 ±0.20

Fig. 3 XAS and XMCD characterization of ***m*CB-NdYb**. Normalized, background-subtracted XAS and XMCD spectra measured across the $M_{4,5}$ edge of Nd (a) and Yb (b) at 6 T and 5 K; (c) field-dependence of the total magnetic moment, $m_{TOT}(H)$/ion, obtained for Nd^{3+} and Yb^{3+}, and magnetic moment per formula unit, at 5.0 K. Open symbols show, for comparison, the magnetization curve $M(H)$ of the mixed MOF determined by SQUID at the same temperature. Table: number of holes (n_h), orbital (m_L), spin (m_S) and total ($m_{TOT} = m_L + m_S$) magnetic moment per Ln(III) ion calculated from the sum rules at 6 T and 5 K.

Dynamic magnetic properties

Ac susceptibility measurements were conducted to study the spin magnetic relaxation properties of all studied compounds. The out-of-phase component of the susceptibility, measured as a function of the frequency at constant temperature (T = 2 K) and different applied magnetic fields, $\chi''(f, H)$, as well as $\chi''(f, T)$ at the optimum field (where the signal is maximized) and varying temperatures, is shown for homonuclear ***m*CB-Ln** (Ln = Nd, Yb) in Fig. 4 and for ***m*CB-NdYb** MOF in Fig. 5 (top). The dependence of the relaxation time on the inverse

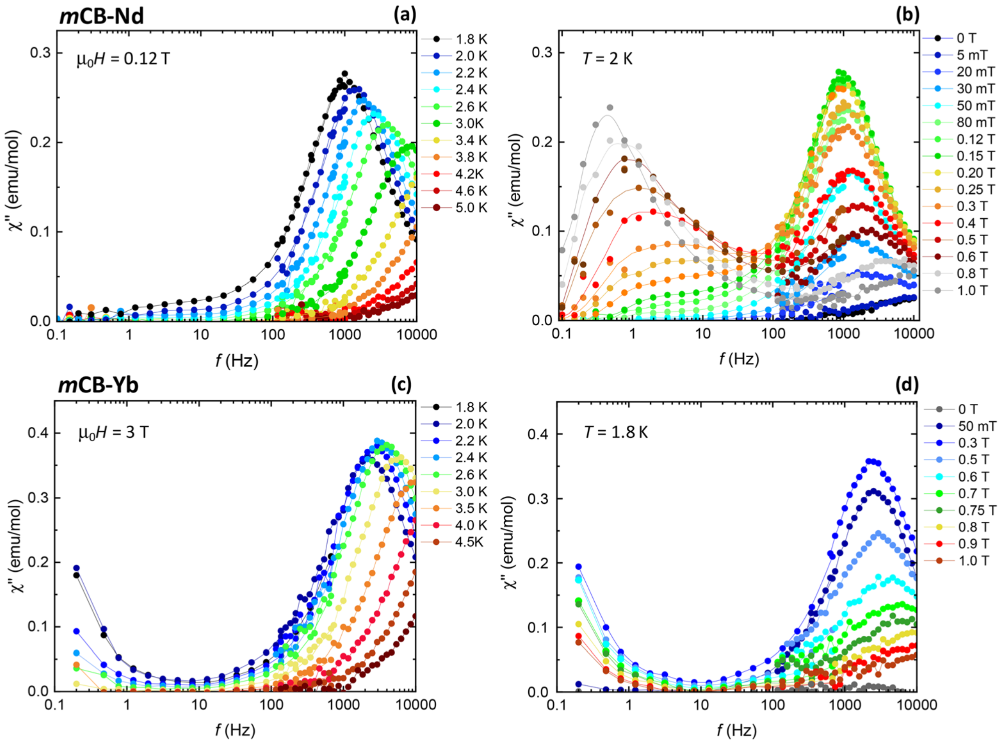

Fig. 4 Ac susceptibility characterization of ***m*CB-Ln** (Ln = Nd, Yb). Out-of-phase component of the ac susceptibility as a function of the frequency, $\chi''(f)$, at constant given field and different temperatures (left: a, c) and at constant T = 2 K and different applied magnetic fields (right: b, d). Lines are guides for the eye.

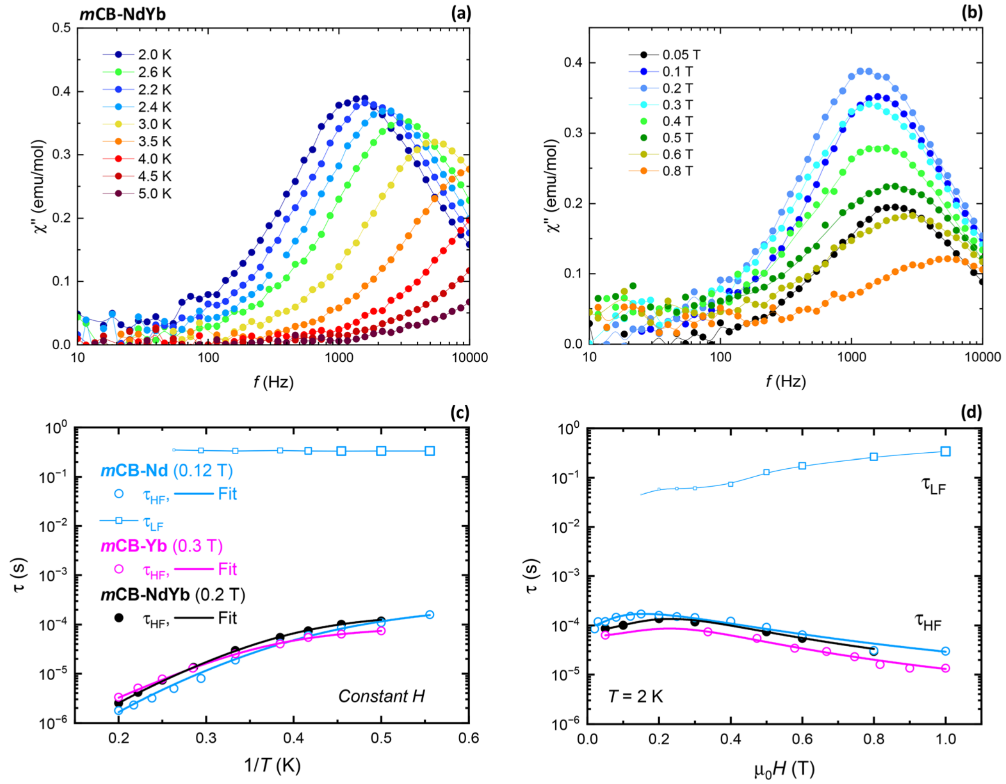

Fig. 5 Dynamic properties of *m*CB-based {Nd/Yb} MOFs. Top: Out-of-phase component of the ac susceptibility as a function of the frequency, $\chi''(f)$, at 2 T and different temperatures (a), and at constant $T = 2$ K and different applied magnetic fields (b) for ***m*CB-NdYb**. Bottom: Magnetic relaxation time as a function of the inverse temperature, $\tau(1/T)$, at constant, given magnetic field (c), and as a function of the field, $\tau(H)$, at $T = 2$ K (d), for ***m*CB-Ln** (Ln = Nd, Yb) (open symbols) and ***m*CB-NdYb** (bold symbols). Fit of the high-frequency process relaxation time data, $\tau_{\mathrm{HF}}(1/T)$ and $\tau_{\mathrm{HF}}(H)$, to the theoretical expression eqn (1) with parameters summarized in Table 1.

temperature, $\tau(1/T)$, and on the magnetic field, $\tau(H)$, determined from the positions of $\chi''(f)$ peaks for each compound, is shown in Fig. 5 (bottom).

For all compounds, no χ'' signal was observed at $H = 0$, even at 2 K, indicating the presence of a quantum tunneling of the magnetization (QTM) mechanism with a relaxation time $\tau_{\mathrm{QT}} < 10^{-5}$ s faster than the maximum frequency of the experiment window ($0.01 < f < 10$ kHz). The application of an external field $H \neq 0$ quenches the QTM process and allows slow relaxation to be observed in all compounds (Fig. 4 and 5).

For ***m*CB-Nd**, the $\chi''(f, H, 2\ \mathrm{K})$ data exhibits a high-frequency-peak (HF) at *ca.* 1000 Hz and a low-frequency (LF) peak at ~1 Hz, evidencing the existence of two distinct relaxation paths (Fig. 4b). No intensity associated with the LF process is observed in the $\chi''(f, T)$ data at 0.12 T (Fig. 4a). The relaxation time dependencies, $\tau_{\mathrm{LF}}(1/T)$ and $\tau_{\mathrm{LF}}(H)$, are characteristic of a direct process affected by phonon-bottleneck (PB) effect. This collective PB phenomenon arises when the energy of the lattice modes generated by the relaxing spins cannot be released into the thermal bath at sufficiently high rate.[129] Such behavior has been previously reported in a wide variety of molecular[130] and metal–organic compounds of various dimensionalities,[42,90,131] and in particular in the isostructural ***m*CB-Ln** (Ln = Dy, Tb,[132] 8RE[80]) MOF analogues of this family. For ***m*CB-Yb**, the $\chi''(f, T, 0.3\ \mathrm{T})$ and $\chi''(f, H, 2\ \mathrm{K})$ curves display a main HF peak (Fig. 4c and d) along with the tails of a second, slower LF peak <0.01 Hz. For the mixed ***m*CB-NdYb** MOF, the dynamics of the main, HF peak are clearly observable in the $\chi''(f, T, 0.2\ \mathrm{T})$ and $\chi''(f, H, 2\ \mathrm{K})$ curves shown in (Fig. 5a and b).

The temperature and field dependence of the HF relaxation time for the three studied MOFs was analyzed using the equation:

$$\tau_{\mathrm{HF}}^{-1} = \frac{B_1}{1 + B_2H^2} + D_1H^4T + D_2H^4T + CT^n + \tau_0^{-1}\exp(-U/k_{\mathrm{B}}T), \qquad (1)$$

where the first term accounts for the field dependence of the QTM process, the second (third) terms describe the direct process for a Kramers ion without (with) hyperfine interactions, the fourth represents Raman relaxation, and the last term corresponds to thermally-activated Orbach relaxation. To avoid over parametrization, we first fitted $\tau_{\mathrm{HF}}(H)$ to determine B_1, B_2, D_1, D_2, and then fitted $\tau_{\mathrm{HF}}(1/T)$ curves at fixed field to extract the Raman (C, n) and Orbach (τ_0, U) parameters. As shown in Fig. 5c and d, the $\tau(H, T)$ curves for all compounds could be well reproduced using the fitting parameters summarized in Table 1. For completeness, we also attempted to fit the $\tau_{\mathrm{HF}}(1/T)$ and $\tau_{\mathrm{HF}}(H)$ data excluding the thermally activated term; however, the reduced model provides a less satisfactory description

Table 1 Parameters obtained from fitting the relaxation time data in Fig. 5c and d using eqn (1)

MOF	Dependence	B_1 (s^{-1})	B_2 (T^{-2})	D_2 (s^{-1} K^{-1} T^{-2})	C (s^{-1} K^{-n})	n	τ_0 (s)	U/k_B (K)
***m*CB-Nd**	$\tau_{HF}{}^{-1}(H)$, 2 K	6380	2.6×10^2	141×10^2	113	5	8.2×10^{-8}	19.8
	$\tau_{HF}{}^{-1}(1/T)$, 0.12 T	6380	2.6×10^2	1024×10^2	117	5	8.2×10^{-8}	19.8
***m*CB-Yb**	$\tau_{HF}{}^{-1}(H, 1/T)$	16 085	0.23×10^2	420×10^2	0	(7)	8.7×10^{-8}	18.4
***m*CB-NdYb**	$\tau_{HF}{}^{-1}(H, 1/T)$	110 395	0.35×10^2	218×10^2	14.9	5.8	1.01×10^{-7}	18.8

of the overall experimental relaxation data (see Fig. S6 and Table S7).

For the homonuclear compounds, the determined Orbach energy barriers, U/k_B = 19.8 K (***m*CB-Nd**) and U/k_B = 18.4 K (***m*CB-Yb**), are similar and close to that of the mixed ***m*CB-NdYb** MOF (U/k_B = 18.8 K) within experimental uncertainty. For ***m*CB-Yb** and ***m*CB-NdYb** MOFs, eqn (1) satisfactorily reproduces both the H and T dependences of the relaxation time. The τ_{HF} decreases as H^{-2}, as expected for a Kramers doublet with some effect of hyperfine interaction ($D_2 \neq 0$). The Raman exponent found for the Nd MOF is $n \approx 5$, within the range of values typically reported for Nd ions, whereas for the Yb compound, the Raman contribution is negligible. In contrast, for ***m*CB-Nd** the $\tau_{HF}(H)$ and $\tau_{HF}(1/T)$ dependencies could only be fitted independently but not with a single set of parameters. This behavior, previously reported in other Nd-compounds,[90] may be explained by the presence of Nd–Nd interactions, which are not accounted for in the single-ion relaxation model implicit in

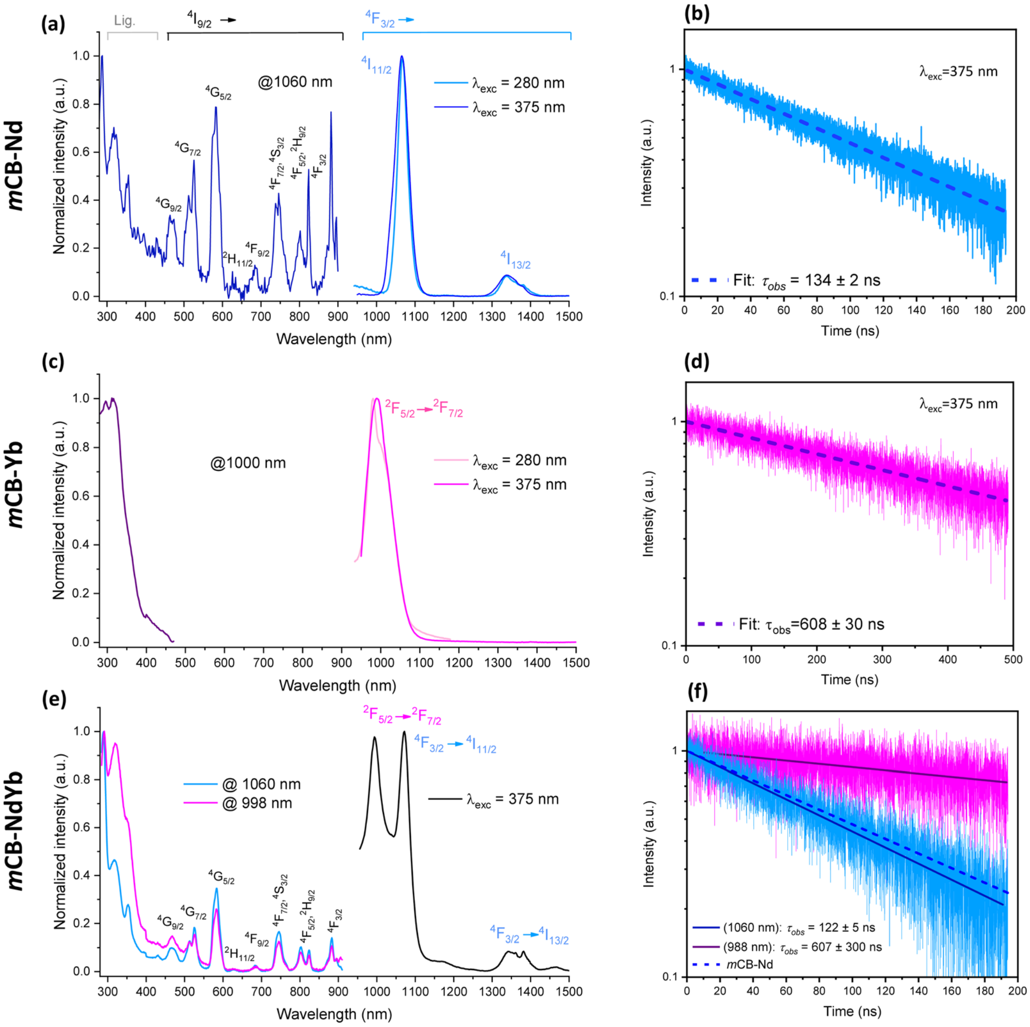

Fig. 6 Photoluminescent properties of ***m*CB-Ln** (Ln = Nd, Yb) and mixed ***m*CB-NdYb** MOFs. Top panel (***m*CB-Nd**): (a) normalized excitation spectrum (λ_{mon} = 1060 nm) and emission spectrum (λ_{exc} = 280 nm and 375 nm); (b) excited state decay measured at 1060 nm. Middle panel (***m*CB-Yb**): (c) normalized excitation spectrum (λ_{mon} = 1000 nm) and emission spectrum (λ_{exc} = 280 nm and 375 nm); (d) excited state decay measured at 1000 nm. Bottom panel (***m*CB-NdYb**): (e) normalized excitation spectrum (λ_{mon} = 1060 nm and λ_{mon} = 1000 nm) and emission spectrum (λ_{exc} = 375 nm); (f) excited state decay measured at 1060 nm and 1000 nm.

eqn (1); such interactions can act as an effective internal magnetic field, modifying the $\tau(H)$ dependence compared to that of isolated ions. Consistent with this interpretation, the mixed ***m*CB-NdYb** (where XMCD indicate negligible Nd–Yb coupling), exhibits $\tau(H)$ and $\tau(T)$ data that can be fitted by a common parameter set.

Optical properties

The photophysical behavior of ***m*CB-Ln** (Ln = Nd, Yb) and mixed ***m*CB-NdYb** MOFs was investigated through solid-state emission and excitation spectroscopy, along with lifetime decay measurements at room temperature. In a previous study, we established the energy of the triplet state (T_1) of the *m*CB ligand to be 23 593 cm^{-1},[133] *a priori* sufficiently high to sensitize the $^4F_{3/2}$ state of Nd^{3+} (~11 260 cm^{-1}) and the $^2F_{5/2}$ state of Yb^{3+} (~10 250 cm^{-1}).[117]

The photoluminescence spectrum of ***m*CB-Nd** upon ligand excitation exhibits the characteristic Nd^{3+} transitions in the NIR range at 1060 nm and 1334 nm assigned to $^4F_{3/2} \rightarrow {}^4I_J$ (J = 11/2, 13/2), respectively (Fig. 6a). We note that the transition to the $^4I_{9/2}$ state, expected at 880 nm, could not be recorded due to our NIR spectrometer being limited to above 900 nm. The excitation spectrum, monitored at λ_{em} = 1060 nm, shows the sensitization of both the ligand (~300 nm) and direct f–f transitions, identified in Fig. 6a. The lifetime value monitored at 1060 nm was found to be τ = 134 ns (Fig. 6b).

On the other hand, the emission spectrum of the ***m*CB-Yb** compound upon ligand excitation shows the expected Yb^{3+} band with a maximum at 1000 nm, assigned to $^2F_{5/2} \rightarrow {}^2F_{7/2}$ transition (Fig. 6c). The excited-state lifetime decay was found to be 608 ns (Fig. 6d). The excitation spectrum (λ_{em} = 1000 nm) exhibits essentially the sensitization of the ligand (Fig. 6c) and no sharp features, as Yb^{3+} does not possess any electronic levels in the UV-vis range.

The above data confirms that sensitization of the different NIR-emitting Ln^{3+} ions occur through the ligand's electronic states *via* the antenna effect, however, the excited-state lifetimes are sensibly shorter than that observed for Eu, Tb.[133]

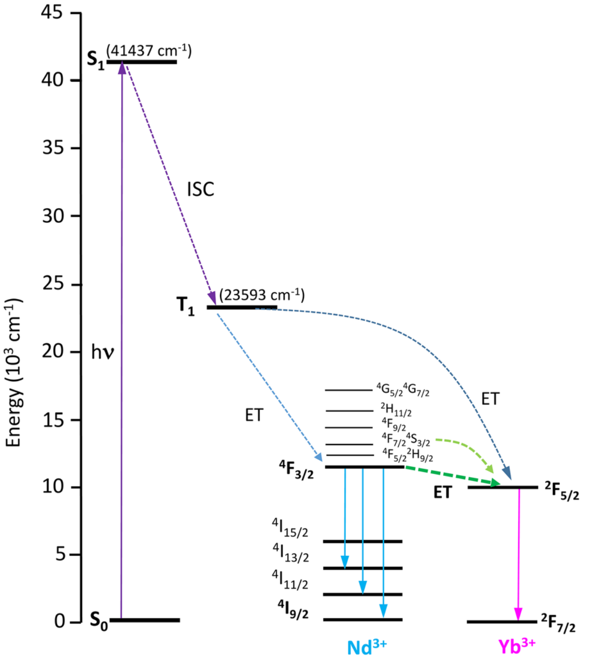

Fig. 7 Schematic of energy transfer in *m*CB-{Nd/Yb} MOFs. Schematic diagram of the light absorption from the singlet state (S_0) to the singlet excited state (S_1) of the *m*CBL ligand, transfer to the triplet state (T_1) by intersystem crossing (ISC) and energy transfer (ET) to the low-lying excited states of Nd^{3+} or Yb^{3+}. ET occurs to the excited $^2F_{5/2}$ (***m*CB-Nd**) or $^2F_{3/2}$ (***m*CB-Yb**) levels, leading to emission, with additional Nd-to-Yb energy transfer channels[119] (dotted green arrows) for ***m*CB-NdYb**.

The mixed ***m*CB-NdYb** provides a suitable platform to probe intramolecular energy transfer (ET) from Nd^{3+} to Yb^{3+}. Upon ligand excitation, the emission spectrum of ***m*CB-NdYb** (Fig. 6e) reveals characteristic emission bands from both Nd^{3+} ($^4F_{3/2} \rightarrow {}^4I_{11/2}$ and $^4F_{3/2} \rightarrow {}^4I_{13/2}$) and Yb^{3+} ($^2F_{5/2} \rightarrow {}^2F_{7/2}$). Time-resolved measurements yield lifetimes of 122 ns for Nd^{3+} (monitored at 1060 nm) and 607 ns for Yb^{3+} (at 1000 nm), (Fig. 6f). Compared to the homometallic analogues, these values indicate a small decrease in the Nd^{3+} lifetime and retention of the Yb^{3+} decay time, consistent with partial Nd-to-Yb energy transfer. A schematic representation of the ET phenomena in the mixed MOF ***m*CB-NdYb** is shown in (Fig. 7). The Ln-to-Ln energy transfer efficiency can be calculated as $\eta_{ET} = 1 - \tau_{DA}/\tau_D$, where τ_D and τ_{DA} are the lifetimes of the emitting level of the donor in the absence and presence of acceptors, respectively. Applying this model, we obtain an ET efficiency of only $\eta_{ET} \sim 9\%$. Known factors influencing ET efficiency include the framework rigidity, spatial distribution of donor and acceptor ions,[116] and their interionic distances.[121] Prior studies on mixed Nd/Yb MOFs with varying metal ratios identified a Nd : Yb = 1 : 1 as optimal, as it minimizes Nd–Nd and Yb–Yb self-quenching interactions.[120,122] Since ***m*CB-NdYb** already features this ideal composition, the modest ET efficiency likely arises from other factors. Specifically, the Nd–Yb distances in this MOF exceed 4.6 Å along the chains and reach 11–17 Å between chains—significantly larger than in mixed molecules such as [NdYb] ($\eta_{ET} \approx 45\%$, $d \approx 3.8$ Å)[115] and [YbNdYb] ($\eta_{ET} \approx 89\%$, $d \approx 3.9$ Å),[117] where shorter intermetallic distances favor more efficient ET. Furthermore, recent studies[119] have shown that the commonly used $\eta_{ET} = 1 - \tau_{DA}/\tau_D$, based on the Nd^{3+} $^4F_{3/2}$ level, may significantly underestimate the true ET efficiency—or even be inadequate—when ET pathways involving this level account only for a small fraction of the overall Nd^{3+}-to-Yb^{3+} process. Overall, the modest ET efficiency observed in ***m*CB-NdYb** likely reflects both the large Nd–Yb separations and the limitations of the simple lifetime-based model; further understanding of the ET mechanism would require advanced theoretical modeling, as recently demonstrated,[119] beyond the scope of this work.

We further probed ET by comparing the excitation spectra of ***m*CB-NdYb**—monitored at both Nd^{3+} (1060 nm) and Yb^{3+} (980 nm) emissions—with those of the homometallic analogues (Fig. 6e). The spectrum at 1060 nm coincides exactly with that of ***m*CB-Nd** (Fig. 6a), with bands corresponding to Nd^{3+} $^4F_{9/2}$ to higher excited states. Crucially, the excitation profile at 980 nm shows the same Nd^{3+} absorption lines, unambiguously demonstrating that Yb^{3+} emission is sensitized by Nd^{3+} excitation *via* Nd-to-Yb energy transfer.

Conclusions

We have reported the synthesis and full structural, magneto-thermal and optical properties of novel carborane-based MOFs $\{[(Nd_yYb_{1-y})_3(m\text{CB-L})_4(NO_3)(DMF)_x]_n\cdot\text{Solv}\}$, including homometallic Nd (y = 1) and Yb (y = 0), as well as the mixed Nd/Yb analogue (y = 0.44). The bulky and acidic *m*CB-L ligand provides an efficient platform for producing isostructural multivariate MOFs with tunable lanthanide combinations and compositions, thus enabling the rational design of materials with targeted properties. All three MOFs are multifunctional, combining field-induced slow relaxation of the magnetization ($U/k_B \approx 19$ K), appreciable magnetocaloric effects ($-\Delta S_M \sim 1.6R$ at 5 T, 1.8 K) and near-infrared (NIR) luminescence. Remarkably, the mixed Nd/Yb MOF uniquely exhibits dual NIR emission ($\approx$998 and 1060 nm) arising from partial Nd → Yb energy transfer, thereby expanding the multifunctionality potential. Element-selective XAS-XMCD measurements on ***m*CB-NdYb** confirmed the trivalent states of Nd^{3+} and Yb^{3+} ions and enabled extraction of their spin, orbital and total magnetic moments, as well as their individual $m_{TOT}(H)$ contributions to the bulk magnetization. By establishing composition–property correlations in the underexplored family of Nd/Yb systems, this work advances the development of multifunctional Ln-MOFs, and opens opportunities in materials for quantum technologies, optical communication, and cryogenic cooling technologies.

Beyond the specific Nd/Yb system studied here, our results demonstrate that carborane-based linkers provide a versatile synthetic route to multi-lanthanide MOFs, enabling advanced hybrid materials with tailored or synergistic functionalities. Importantly, broadening the library of well-characterized multimetallic MOFs is a key step toward data-driven discovery approaches, including AI-guided design of novel functional MOFs.

Author contributions

X. L.: investigation, formal analysis, data curation, visualization; A.A.: investigation, resources, methodology; S. F.: investigation, resources, formal analysis; J. G. P.: supervision, methodology, investigation, resources, funding acquisition; E. B.: project administration, conceptualization, supervision, methodology, investigation, resources, formal analysis, data curation, visualization, funding acquisition, writing – original draft, review and editing. All authors discussed the results and contributed to revising the manuscript.

Conflicts of interest

There are no conflicts to declare.

Data availability

All relevant data are within the manuscript and its supplementary information (SI). Supplementary information: (S1) summary of Nd(III) compounds with SMM and/or NIR behavior; (S2) summary of Yb(III) compounds with SMM and/or NIR behavior; (S3) summary of mixed Nd(III)/Yb(III) compounds with SMM and/or NIR behavior; (S4) chemical and structural characterization; (S5) additional magnetic data. See DOI: https://doi.org/10.1039/d5tc03820k.

Acknowledgements

This work was financially supported by MCIU (PID2022-138492NB-I00), PID2021-122869NB-I00 and PID2022-136892NB-I00, the Generalitat de Catalunya (2021/SGR/00442), and the Gobierno de Aragón (RASMIA E12-23 and E17-23R). EB and JGP acknowledges financial support from the State Investigation Agency, through the Severo Ochoa Programme for Centres of Excellence in R&D (CEX2023-001263-S). Xiaoming Liu is enrolled in the UAB PhD program and acknowledges the China Scholarship Council (CSC) for his PhD grant (202306450070). Authors would like to acknowledge the use of Servicio General de Apoyo a la Investigación-SAI, Universidad de Zaragoza. XAS and XMCD experiments were performed at the BOREAS beamline of the ALBA synchrotron with the support of ALBA staff (experiment number experiment 2023087679).

References

1 X. J. Wang, X. Zhang, R. Pandharkar, J. F. Lyu, D. Ray, Y. Yang, S. Kato, J. Liu, M. C. Wasson, T. Islamoglu, Z. Li, J. T. Hupp, C. J. Cramer, L. Gagliardi and O. K. Farha, *ACS Catal.*, 2020, **10**, 8995–9005.
2 A. Bavykina, N. Kolobov, I. S. Khan, J. A. Bau, A. Ramirez and J. Gascon, *Chem. Rev.*, 2020, **16**, 8468–8535.
3 D. Q. Yuan, D. Zhao, D. F. Sun and H. C. Zhou, *Angew. Chem.*, 2010, **49**, 5357–5361.
4 O. M. Yaghi, N. W. Ockwig, H. K. Chae, M. Eddaoudi and J. Kim, *Nature*, 2003, **423**, 705–714.
5 B. Li, H. M. Wen, W. Zhou and B. Chen, *J. Phys. Chem. Lett.*, 2014, **5**(20), 3468–3479.
6 D. Wang, H. Yao, J. Ye, Y. Gao, H. Cong and B. Yu, *Small*, 2024, **20**(47), 2404350.
7 X. Zhang, V. Vieru, X. Feng, J.-L. Liu, Z. Zhang, B. Na, W. Shi, B.-W. Wang, A. K. Powell, L. F. Chibotaru, S. Gao, P. Cheng and J. R. Long, *Angew. Chem.*, 2015, **54**, 9861–9865.
8 K. Liu, X. Zhang, X. Meng, W. Shi, P. Cheng and A. K. Powell, *Chem. Soc. Rev.*, 2016, **45**, 2423–2439.
9 G. Mínguez Espallargas and E. Coronado, *Chem. Soc. Rev.*, 2018, **47**, 533–557.
10 Y. Cui, B. Chen and G. Qian, *Coord. Chem. Rev.*, 2014, **273–274**, 76–86.
11 Z. Qu, D. Wu, J. Jin, G. Yang and Y.-Y. Wang, *J. Solid State Chem.*, 2022, **309**, 123003.

12 Y. J. Son, D. Kim, J. W. Park, Y. Yu and S. J. Hwang, *Coord. Chem. Rev.*, 2025, **526**, 216317.

13 Z. Li, R. Núñez, M. E. Light, E. Ruiz, F. Teixidor, C. Viñas, D. Ruiz-Molina, C. Roscini and J. G. Planas, *Chem. Mater.*, 2022, **34**, 4795–4808.

14 Y. Guo, Z. Han, H. Min, Z. Chen, T. Sun, L. Wang, W. Shi and P. Cheng, *Inorg. Chem.*, 2021, **60**, 9192–9198.

15 J.-M. Li, R. Huo, X. Li and H.-L. Sun, *Inorg. Chem.*, 2019, **58**, 9855–9865.

16 Q. Lin, W. Xie, Z. Zong, Z. Liu, Y. Sun and L. Liang, *New J. Chem.*, 2021, **45**, 7382–7389.

17 S. Mohapatra, B. Rajeswaran, A. Chakraborty, A. Sundaresan and T. K. Maji, *Chem. Mater.*, 2013, **25**, 1673–1679.

18 D. B. Kanzariya, M. Y. Chaudharya and T. K. Pal, *Dalton Trans.*, 2023, **52**, 7383–7404.

19 G. Lorusso, J. W. Sharples, E. Palacios, O. Roubeau, E. K. Brechin, R. Sessoli, A. Rossin, F. Tuna, E. J. L. McInnes, D. Collison and M. Evangelisti, *Adv. Mater.*, 2013, **25**, 4653–4656.

20 G. Lorusso, E. Natividad, M. Evangelisti and O. Roubeau, *Mater. Horiz.*, 2019, **6**, 144–156.

21 M. Falsaperna and P. Saines, *Dalton Trans.*, 2022, **51**, 3394–3410.

22 P. Konieczny, W. Sas, D. Czernia, A. Pacanowska, M. Fitta and R. Pełka, *Dalton Trans.*, 2022, **51**, 12762–12780.

23 E. Coronado, *Nat. Rev. Mater.*, 2020, **5**, 87–104.

24 M. J. Graham, J. M. Zadrozny, M. S. Fataftah and D. E. Freedman, *Chem. Mater.*, 2017, **29**, 1885–1897.

25 C. Zhang, X. Ma, P. Cen, X. Jin, J. Yang, A. Y.-Q. Zhang, J. Ferrando-Soria, E. Pardo and X. Liu, *Dalton Trans.*, 2020, **49**, 14123–14132.

26 L. Li, Y. Fang, S. Liu, M. Hu and W. Wang, *J. Rare Earths*, 2023, **41**, 100–107.

27 C. Bai, C.-T. Li, H.-M. Hu, B. Liu, J.-D. Li and G. Xue, *Dalton Trans.*, 2019, **48**, 814–817.

28 Z. Chen, B. Zhao, P. Cheng, X. Q. Zhao, W. Shi and Y. Song, *Inorg. Chem.*, 2009, **48**, 3493–3495.

29 T. Yang, S. Wang, C. Lin, X. Wang, B. Zhu and D. Wu, *Dalton Trans.*, 2021, **50**, 1293–1299.

30 A. Calahorro, I. Oyarzabal, B. Fernandez, J. Seco, T. Tian and D. Fairen-Jimenez, *Dalton Trans.*, 2016, **45**, 591–598.

31 R. Gao, F. Guo, N. Bai, Y. Wu, F. Yang and J. Liang, *Inorg. Chem.*, 2016, **55**, 11323–11330.

32 J. López-Cabrelles, L. Escalera-Moreno, Z. Hu, H. Prima-García, G. Mínguez-Espallargas, A. Gaita-Ariño and E. Coronado, *Inorg. Chem.*, 2021, **60**, 8575–8580.

33 A. Urtizberea, E. Natividad, P. J. Alonso, M. A. Andrés, I. Gascón, M. Goldmann and O. Roubeau, *Adv. Funct. Mater.*, 2018, **28**, 1801695.

34 E. Bartolomé, X.-B. Li, A. Arauzo, J. Luzón, I. García-Rubio and J. Giner Planas, *ACS Appl. Mater. Interfaces*, 2025, **17**, 42082–42095.

35 N. Ishikawa, M. Sugita, T. Ishikawa, S. Y. Koshihara and Y. Kaizu, *J. Am. Chem. Soc.*, 2003, **125**, 8694–8695.

36 E. Bartolomé, A. Arauzo, J. Luzón, J. Bartolomé and F. Bartolomé, in *Handbook of Magnetic Materials*, ed. E. Brück, Elsevier, 2017, pp. 1–289.

37 L. Sorace and D. Gatteschi, in *Lanthanides and Actinides in Molecular Magnetism*, ed. R. Layfield and M. Murugesu, Wiley-VCH, 2015.

38 R. J. C. Dixey and P. J. Saines, *Inorg. Chem.*, 2018, **57**, 12543–12551.

39 P. J. Saines, J. A. M. Paddison, P. M. M. Thygesen and M. G. Tucker, *Mater. Horiz.*, 2015, **2**, 528–535.

40 P. W. Doheny, S. J. Cassidy and P. J. Saines, *Inorg. Chem.*, 2022, **61**, 4957–4964.

41 S. Kim, R. Muhammad, K. Son and H. Oh, *Inorg. Chem.*, 2023, **62**, 2994–2999.

42 J. González, P. Sevilla, G. Gabarró-Riera, J. Jover, J. Echeverría, S. Fuertes, A. Arauzo, E. Bartolomé and E. C. Sañudo, *Angew. Chem.*, 2021, **60**, 12001–12006.

43 E. Bartolomé, A. Arauzo, S. Fuertes, L. Navarro-Spreafica, P. Sevilla, H. F. Cortés, N. Settineri, S. J. Teat and E. C. Sañudo, *Dalton Trans.*, 2023, **52**, 7258–7270.

44 F.-G. Chen, W. Xu, J. Chen, H.-P. Xiao, H.-Y. Wang, Z. Chen and J.-Y. Ge, *Inorg. Chem.*, 2022, **61**, 5388–5396.

45 X.-Q. Ji, R. Sun, J. Xiong, H.-L. Sun and S. Gao, *J. Mater. Chem. C*, 2021, **9**, 15858–15867.

46 R. E. Sikma, K. S. Butler, D. J. Vogel, J. A. Harvey and D. F. Sava Gallis, *J. Am. Chem. Soc.*, 2024, **146**, 5715–5734.

47 W. Jiang, C.-C. Liang and Y.-B. Zhang, *Adv. Funct. Mater.*, 2024, 2308946.

48 M. Viciano-Chumillas, X. Liu, A. Leyva-Pérez, D. Armentano, J. Ferrando-Soria and E. Pardo, *Coord. Chem. Rev.*, 2022, **451**, 214273.

49 C. Castillo-Blas, V. A. De la Peña-O'Shea, I. Puente-Orench, J. Romero de la Paz, R. Sáez-Puche, R. Gutierrez-Puebla and F. Gándara, *Sci. Adv.*, 2017, **3**, e1700773.

50 K. L. S. Abednatanzi, P. G. Derakhshandeh, H. Depauw, F.-X. Coudert, H. Vrielinck and P. Van Der Voort, *Chem. Soc. Rev.*, 2019, **48**, 2535–2565.

51 Y. Wang, Y.-Y. Xue, L.-T. Yan, H.-P. Li, Y.-P. Li, E.-H. Yuan, M. Li, S.-N. Li and Q.-G. Zhai, *ACS Appl. Mater. Interfaces*, 2020, **12**, 24786.

52 L. J. Wang, H. Deng, H. Furukawa, F. Gándara, K. E. Cordova, D. Peri and O. M. Yaghi, *Inorg. Chem.*, 2014, **53**, 5881.

53 X. Zhao, Z. Xue, W. Chen, X. Bai, R. Shi and T. Mu, *J. Mater. Chem. A*, 2019, **7**, 26238.

54 R. L. Vasile, A. A. Godoy, I. Puente Orench, N. M. Nemes, V. A. de la Peña O'Shea, E. Gutiérrez-Puebla, J. L. Martínez, M. Á. Monge and F. Gándara, *Chem. Mater.*, 2022, **34**, 7029–7041.

55 H. Brunckova, E. Mudra, L. Rocha, E. Nassar, W. Nascimento, H. Kolev, M. Lisnichuk, A. Kovalcikova, Z. Molcanova, M. Strečkova and L. Medvecky, *Inorganics*, 2021, **9**, 77.

56 X. Fan, S. Freslon, C. Daiguebonne, G. Calvez, L. Le Pollès, K. Bernot and O. Guillou, *J. Mater. Chem. C*, 2014, **2**, 5510–5525.

57 A. E. Psalti, D. Andriotou, S. A. Diamantis, A. Chatz-Giachia, A. Pournara, M. J. Manos, A. Hatzidimitriou and T. Lazarides, *Inorg. Chem.*, 2022, **61**, 11959–11972.

58 Y. Zheng, K. Liu, X. Sun, R. Guan, H. Su, H. You and C. Qi, *CrystEngComm*, 2015, **17**, 2321.

59 T. Alammar, I. Z. Hlova, S. Gupta, A. Biswas, T. Ma, L. Zhou, V. Balema, V. K. Pecharsky and A.-V. Mudring, *New J. Chem.*, 2020, **44**, 1054.

60 H. Brunckova, E. Mudra, L. Rocha, E. Nassar, W. Nascimento, H. Kolev, A. Kovalcikova, Z. Molcanova, M. Podobova and L. Medvecky, *Appl. Surf. Sci.*, 2021, **542**, 148731.

61 J. Rong, W. Zhang and J. Bai, *RSC Adv.*, 2016, **6**, 103714.

62 Y. Yang, L. Chen, F. Jiang, M. Yu, X. Wan, B. Zhangab and M. Hong, *J. Mater. Chem. C*, 2017, **5**, 1981.

63 Y. Zhao and D. Li, *J. Mater. Chem. C*, 2020, **8**, 12739–12754.

64 A. Cadiau, C. D. S. Brites, P. M. F. J. Costa, R. A. S. Ferreira, J. Rocha and L. D. Carlos, *ACS Nano*, 2013, **7**, 7213–7218.

65 D. Zhao, X. Rao, J. Yu, Y. Cui, Y. Yang and G. Qian, *Inorg. Chem.*, 2015, **54**, 11193–11199.

66 T. Xia, J. Wang, K. Jiang, Y. Cui, Y. Yang and G. Qian, *Chin. Chem. Lett.*, 2018, **29**, 861–864.

67 Z. Li, A. Arauzo, C. Roscini, J. G. Planas and E. Bartolomé, *J. Mater. Chem. A*, 2024, **12**, 21971–21986.

68 J. I. Deneff, L. E. S. Rohwer, K. S. Butler, B. Kaehr, D. J. Vogel, T. S. Luk, R. A. Reyes, A. A. Cruz-Cabrera, J. E. Martin and D. F. Sava Gallis, *Nat. Commun.*, 2023, **14**, 981.

69 B. P. Dash, R. Satapathy, J. A. Maguire and N. S. Hosmane, *New J. Chem.*, 2011, **35**, 1955–1972.

70 M. Scholz and E. Hey-Hawkins, *Chem. Rev.*, 2011, **111**, 7035–7062.

71 F. Issa, M. Kassiou and L. M. Rendina, *Chem. Rev.*, 2011, **111**, 5701–5722.

72 J. Plesek, *Chem. Rev.*, 1992, **92**, 269–278.

73 R. N. Grimes, *Carboranes*, Academic Press, 2016.

74 F. Teixidor and D. E. Kaufmann, *Science of Synthesis: Houben-Weyl Methods of Molecular Transformations*, Georg Thieme Verlag, Stuttgart, 5th edn, 2015, vol. 6.

75 S. Fujii, *MedChemComm*, 2016, **7**, 1082–1092.

76 J. F. Valliant, K. J. Guenther, A. S. King, P. Morel, P. Schaffer, O. O. Sogbein and K. A. Stephenson, *Coord. Chem. Rev.*, 2002, **232**, 173–230.

77 J. Poater, C. Viñas, I. Bennour, S. Escayola, M. Solà and F. Teixidor, *J. Am. Chem. Soc.*, 2020, **142**, 9396–9407.

78 J. Poater, M. Solà, C. Viñas and F. Teixidor, *Angew. Chem.*, 2014, **53**, 12191–12195.

79 J. Poater, C. Viñas, M. Solà and F. Teixidor, *Nat. Commun.*, 2022, **13**, 3844.

80 Z. Li, X. B. Li, M. E. Light, A. E. Carrillo, A. Arauzo, M. Valvidares, C. Roscini, F. Teixidor, C. Viñas, F. Gándara, E. Bartolomé and J. G. Planas, *Adv. Funct. Mater.*, 2023, **33**(47), 2307369.

81 J. D. Rinehart and J. R. Long, *Dalton Trans.*, 2012, **41**, 13572–13574.

82 J. J. Baldoví, J. M. Clemente-Juan, E. Coronado, Y. Duan, A. Gaita-Ariño and C. Giménez-Saiz, *Inorg. Chem.*, 2014, **53**, 9976–9980.

83 R. Vicente, À. Tubau, S. Speed, F. A. Mautner, F. Bierbaumer, R. C. Fischer and S. S. Massoud, *New J. Chem.*, 2021, **45**, 14713–14723.

84 H. Wada, S. Ooka, T. Yamamura and T. Kajiwara, *Inorg. Chem.*, 2017, **56**, 147–155.

85 S. K. Gupta, T. Rajeshkumar, G. Rajaraman and R. Murugavel, *Chem. Commun.*, 2016, **52**, 7168–7171.

86 J. J. Le Roy, S. I. Gorelsky, I. Korobkov and M. Murugesu, *Organometallics*, 2015, **34**, 1415–1418.

87 B. Casanovas, M. Font-Bardía, S. Speed, M. S. El Fallah and R. Vicente, *Eur. J. Inorg. Chem.*, 2018, 1928–1937.

88 G. Huang, G. Calvez, Y. Suffren, C. Daiguebonne, S. Freslon, O. Guillou and K. Bernot, *Magnetochemistry*, 2018, **4**(4), 44.

89 B. Casanovas, S. Speed, O. Maury, M. S. El Fallah, M. Font-Bardía and R. Vicente, *Eur. J. Inorg. Chem.*, 2018, 3859–3867.

90 E. Bartolomé, A. Arauzo, J. Luzón, S. Melnic, S. Shova, D. Prodius, I. C. Nlebedim, F. Bartolomé and J. Bartolomé, *Dalton Trans.*, 2019, **48**, 15386–15396.

91 A. Zouzou, A. Beghidja, C. Beghidja, Y. Guari, J. Larionova, J. Long and F. Gándara, *Cryst. Growth Des.*, 2021, **21**, 5072–5085.

92 Y. Gao, R. Broersen, W. Hageman, N. Yan, M. C. Mittelmeijer-Hazeleger, G. Rothenberg and S. Tanase, *J. Mater. Chem. A*, 2015, **3**, 22347–22352.

93 R. H. Alzard, S. Alsaedi, S. Alseiari, S. Aljasmi, H. F. El-Maghraby, V. Poulose, A. Hassan, M. Kamel, A. Ali, M. Abdel-Hafiez and M. Abdellah, *ACS Omega*, 2024, **9**, 37386–37395.

94 X. Du and L. Sun, *Inorg. Chem. Front.*, 2024, **11**, 8660–8670.

95 H. H. Yu, J. Li, Y. Yang, X. Li, Z. M. Su and J. Sun, *J. Solid State Chem.*, 2021, **294**, 121789.

96 F. Gándara, A. García-Cortés, C. Cascales, B. Gómez-Lor, E. Gutiérrez-Puebla, M. Iglesias, A. Monge and N. Snejko, *Inorg. Chem.*, 2007, **46**, 3475–3484.

97 T. Qin, F. Cao, W. Zhu, Y. Dai, M. Zhang, Y. Zhang, C. Zhang and J. Wang, *ChemistrySelect*, 2018, **3**, 7871–7875.

98 R. M. Abdelhameed, L. D. Carlos, P. Rabu, S. M. Santos, A. M. S. Silva and J. Rocha, *Eur. J. Inorg. Chem.*, 2014, 5285–5295.

99 R. Jankowski, J. J. Zakrzewski, M. Zychowicz, J. Wang, Y. Oki, S. I. Ohkoshi, S. Chorazy and B. Sieklucka, *J. Mater. Chem. C*, 2021, **9**, 10705–10717.

100 K. Kumar, G. Li, O. Stefanczyk, S. Chorazy, K. Nakabayashi and S. I. Ohkoshi, *J. Mater. Chem. C*, 2023, **11**, 1008–1021.

101 M. V. Marinho, D. O. Reis, W. X. C. Oliveira, L. F. Marques, H. O. Stumpf, M. Déniz, J. Pasán, C. Ruiz-Pérez, J. Cano, F. Lloret and M. Julve, *Inorg. Chem.*, 2017, **56**, 2108–2123.

102 I. Oyarzabal, S. Rojas, A. D. Parejo, A. Salinas-castillo, J. Á. García, J. M. Seco, J. Cepeda and A. Rodríguez-diéguez, *Magnetochemistry*, 2021, **7**(3), 41.

103 M. Sugita, N. Ishikawa, T. Ishikawa, S. Y. Koshihara and Y. Kaizu, *Inorg. Chem.*, 2006, **45**, 1299–1304.

104 W. Huang, J. Xu, D. Wu, X. Huang and J. Jiang, *New J. Chem.*, 2015, **39**, 8650–8657.

105 L. Mandal, S. Biswas, G. Cosquer, Y. Shen and M. Yamashita, *Dalton Trans.*, 2018, **47**, 17493–17499.

106 A. V. Gavrikov, N. N. Efimov, A. B. Ilyukhin, Z. V. Dobrokhotova and V. M. Novotortsev, *Dalton Trans.*, 2018, **47**, 6199–6209.

107 M. E. Boulon, G. Cucinotta, J. Luzon, C. Degl'Innocenti, M. Perfetti, K. Bernot, G. Calvez, A. Caneschi and R. Sessoli, *Angew. Chem., Int. Ed.*, 2013, **52**, 350–354.

108 K. S. Pedersen, J. Dreiser, H. Weihe, R. Sibille, H. V. Johannesen, M. A. Sørensen, B. E. Nielsen, M. Sigrist, H. Mutka, S. Rols, J. Bendix and S. Piligkos, *Inorg. Chem.*, 2015, **54**, 7600–7606.

109 S. P. Petrosyants, K. A. Babeshkin, A. V. Gavrikov, A. B. Ilyukhin, E. V. Belova and N. N. Efimov, *Dalton Trans.*, 2019, **48**, 12644–12655.

110 J. Ruiz, G. Lorusso, M. Evangelisti, E. K. Brechin, S. J. A. Pope and E. Colacio, *Inorg. Chem.*, 2014, **53**, 3586–3594.

111 F. Pointillart, B. Le Guennic, S. Golhen, O. Cador, O. Maury and L. Ouahab, *Chem. Commun.*, 2013, **49**, 615–617.

112 W. Bin Chen, L. Zhong, Y. J. Zhong, Y. Q. Zhang, S. Gao and W. Dong, *Inorg. Chem. Front.*, 2020, **7**, 3136–3145.

113 K. A. Babeshkin, A. V. Gavrikov, S. P. Petrosyants, A. B. Ilyukhin, E. V. Belova and N. N. Efimov, *Eur. J. Inorg. Chem.*, 2020, 4380–4390.

114 A. V. Gavrikov, A. B. Ilyukhin, I. V. Taydakov, M. T. Metlin, N. P. Datskevich, M. E. Buzoverov, K. A. Babeshkin and N. N. Efimov, *Dalton Trans.*, 2023, **52**, 17911–17927.

115 L. Abad Galán, D. Aguilà, Y. Guyot, V. Velasco, O. Roubeau, S. J. Teat, M. Massi and G. Aromí, *Chem. – Eur. J.*, 2021, **27**, 7288–7299.

116 F. Artizzu, A. Serpe, L. Marchiò, M. Saba, A. Mura, M. L. Mercuri, G. Bongiovanni, P. Deplano and F. Quochi, *J. Mater. Chem. C*, 2015, **3**, 11524–11530.

117 D. Maniaki, A. Sickinger, L. A. Barrios Moreno, D. Aguilà, O. Roubeau, N. S. Settineri, Y. Guyot, F. Riobé, O. Maury, L. A. Galán and G. Aromí, *Inorg. Chem.*, 2023, **62**, 3106–3115.

118 D. F. Sava Gallis, L. E. S. Rohwer, M. A. Rodriguez, M. C. Barnhart-Dailey, K. S. Butler, T. S. Luk, J. A. Timlin and K. W. Chapman, *ACS Appl. Mater. Interfaces*, 2017, **9**, 22268–22277.

119 M. Oggianu, V. Mameli, M. A. Hernández-Rodríguez, N. Monni, M. Souto, C. D. S. Brites, C. Cannas, F. Manna, F. Quochi, E. Cadoni, N. Masciocchi, A. N. Carneiro Neto, L. D. Carlos and M. L. Mercuri, *Chem. Mater.*, 2024, **36**, 3452–3463.

120 C. Gu, Y. Ding, X. Quan, M. Gong, J. Yu, D. Zhao and C. Li, *J. Rare Earths*, 2021, **39**, 1024–1030.

121 D. Zhao, J. Zhang, D. Yue, X. Lian, Y. Cui, Y. Yang and G. Qian, *Chem. Commun.*, 2016, **52**, 8259–8262.

122 D. Zhao, X. Han, S. Wang, J. Liu, Y. Lu and C. Li, *Chem. – Eur. J.*, 2020, **26**, 3145–3151.

123 Y. Xin, K. Kumar, J. J. Zakrzewski, S. Chorazy, K. Nakabayashi, O. Stefanczyk and S. I. Ohkoshi, *J. Phys. Chem. C*, 2023, **127**, 15500–15511.

124 M. A. Fox, Icosahedral carborane derivatives, PhD thesis, Durham University, 1991.

125 F. Moro, V. Corradini, M. Evangelisti, R. Biagi, V. De Renzi, U. del Pennino, J. C. Cezar, R. Inglis, C. J. Milios and E. K. Brechin, *Nanoscale*, 2010, **2**, 2698–2703.

126 R. L. Vasile, R. S. Silva, E. Céspedes, J. L. Martínez, E. Gutiérrez-Puebla, M. A. Monge and F. Gándara, *Inorg. Chem.*, 2023, **62**, 19741–19748.

127 S. Tripathi, *Max-Planck-Institut für Intelligente Systeme*, Stuttgart, 2018.

128 B. Thole, P. Carra, F. Sette and G. van der Laan, *Phys. Rev. Lett.*, 1992, **68**, 1943–1946.

129 R. Schenker, M. N. Leuenberger, G. Chaboussant, D. Loss and H. U. Güdel, *Phys. Rev. B: Condens. Matter Mater. Phys.*, 2005, **72**, 184403.

130 M. Goudjil, C. A. Mattei, L. Tacconi, L. Chelazzi and M. Perfetti, *Dalton Trans.*, 2026, **55**, 3336–3445.

131 E. Bartolomé, J. Bartolomé, S. Melnic, D. Prodius, S. Shova, A. Arauzo, J. Luzón, F. Luis and C. Turta, *Dalton Trans.*, 2013, **42**, 10153–10171.

132 Z. Li, A. Arauzo, J. Giner Planas and E. Bartolomé, *Dalton Trans.*, 2024, **53**, 8969–8979.

133 Z. Li, C. Roscini, R. Núñez, F. Teixidor, C. Viñas, E. Ruiz and J. G. Planas, *J. Mater. Chem. C*, 2024, **12**, 2101–2109.